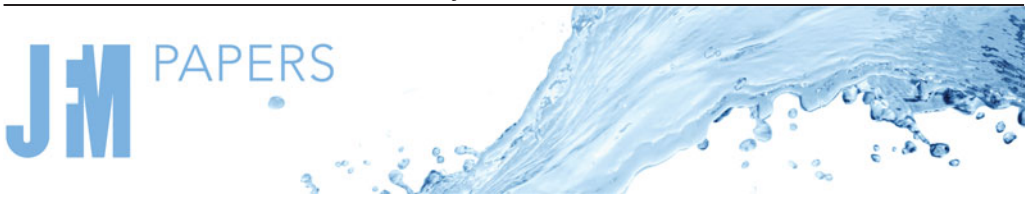
CrossMark

J. Fluid Mech. (2021), *vol*. 915, A51, doi:10.1017/jfm.2021.139



Regularised non-uniform segments and efficient no-slip elastohydrodynamics

B.J. Walker[1],† **and E.A. Gaffney**[1]

[1]Wolfson Centre for Mathematical Biology, Mathematical Institute, University of Oxford, Oxford OX2 6GG, UK

(Received 27 August 2020; revised 27 November 2020; accepted 9 February 2021)

The elastohydrodynamics of slender bodies in a viscous fluid have long been the source of theoretical investigation, being pertinent to the microscale world of ciliates and flagellates as well as to biological and engineered active matter more generally. Although recent works have overcome the severe numerical stiffness typically associated with slender elastohydrodynamics, employing both local and non-local couplings to the surrounding fluid, there is no framework of comparable efficiency that rigorously justifies its hydrodynamic accuracy. In this study, we combine developments in filament elastohydrodynamics with a recent regularised slender-body theory, affording algebraic asymptotic accuracy to the commonly imposed no-slip condition on the surface of a slender filament of potentially non-uniform cross-sectional radius. Further, we do this whilst retaining the remarkable practical efficiency of contemporary elastohydrodynamic approaches, having drawn inspiration from the method of regularised Stokeslet segments to yield an efficient and flexible slender-body theory of regularised non-uniform segments.

Key words: computational methods, slender-body theory

1. Introduction

The coupled elastohydrodynamics of flexible slender filaments are of intense interest to a breadth of active research communities, ranging from theoretical to experimental studies of filaments from the perspectives of synthetic sensors to those rooted in the biology and mechanics of cilia and flagella (Gray 1928; Roper *et al.* 2006; Pozrikidis 2010; Curtis *et al.* 2012; Guglielmini *et al.* 2012; Simons, Fauci & Cortez 2015; Smith, Montenegro-Johnson & Lopes 2019). A comprehensive summary of the field is given in the recent review of du Roure *et al.* (2019), which notes a particular need for further theoretical development in this area. Indeed, up until recently, problems involving filament elastohydrodynamics have been largely out of reach due to the severe numerical stiffness associated with the

† Email address for correspondence: benjamin.walker@maths.ox.ac.uk

© The Author(s), 2021. Published by Cambridge University Press

https://doi.org/10.1017/jfm.2021.139 Published online by Cambridge University Press

dynamics of a slender body in a viscous fluid, with few studies being able to utilise large computing resources to combat this issue (Olson, Lim & Cortez 2013; Ishimoto & Gaffney 2018; Schoeller & Keaveny 2018). However, the work of Moreau, Giraldi & Gadêlha (2018) sought to address such problems, integrating the governing equations of elasticity in space in order to generate a coarse-grained framework with greatly reduced numerical stiffness. Despite being a recent development in the field, this approach has already been extended by Hall-McNair *et al.* (2019) and Walker *et al.* (2019) to include improved non-local hydrodynamics, applied to the model biological problem of flagellar efficiency (Neal *et al.* 2020), and extended to motion in three dimensions (Walker, Ishimoto & Gaffney 2020*b*).

Common to these recent models, as well as to other treatments of slender filaments at zero Reynolds number, are simplified representations of slender-body hydrodynamics. The aforementioned work of Moreau *et al.* (2018) utilises resistive force theory, a local relation between motion and drag that has seen widespread use since its advent in the 1950s (Hancock 1953; Gray & Hancock 1955). More refined and complex are slender-body theories, which capture the non-local coupling of kinematics and associated forces via an integral relation, as considered in the early studies of Keller & Rubinow (1976), Cox (1970) and Lighthill (1976) and later analysed in detail by Johnson (1980). Use of these slender theories in numerical applications often necessitates the use of many-point quadrature rules or specialised techniques to evaluate the integral of a rapidly varying kernel, such as that induced by the cancellation of terms that would otherwise result in singularities (Tornberg & Shelley 2004). Analogous issues of cancelling singularities also plague the numerical performance of methods derived from the boundary integral formulation of the Stokes equations, as summarised by Pozrikidis (1992). In the early 2000s, Cortez (2001) circumvented such issues of numerical complexity by instead considering solutions of the regularly forced Stokes equations, leading to a regularised Green's function and an associated regularised theory. In turn, drawing from significant earlier study of singular slender-body theories, this led to commonplace use of a regularised slender-body theory ansatz for flow around a slender filament in terms of a force density $\boldsymbol{f}$, typically an integral over the centreline of the filament of the form

$$\boldsymbol{u}(\boldsymbol{x}) = \int \boldsymbol{K}^{\epsilon}(\boldsymbol{x}, s')\boldsymbol{f}(s')\,\mathrm{d}s', \tag{1.1}$$

where $\boldsymbol{u}(\boldsymbol{x})$ is the fluid velocity at a point $\boldsymbol{x}$ and $\boldsymbol{K}^{\epsilon}$ is a regular integral kernel. The parameter ϵ represents a length scale of the regularisation and the associated flow-field error, which, in studies of filament dynamics, has often been taken to be the filament radius without rigorous justification (Smith 2009; Cortez & Nicholas 2012; Cortez 2018; Hall-McNair *et al.* 2019; Walker *et al.* 2019), with circular cross-sections invariably assumed. The general ansatz of (1.1) is also commonly used in conjunction with the hydrodynamic no-slip condition, although is evaluated not on the surface of the body, but on the filament centreline. With many approaches taking the integral kernel $\boldsymbol{K}^{\epsilon}$ to simply be the regularised point force Green's function in the appropriate domain, application of this approximate relation does not guarantee that the no-slip boundary condition is satisfied on the surface of the body. Particular issues arise at the endpoints of the filament, where more than a velocity Green's function can be required (Chwang & Wu 1975).

Building upon the singular work of Johnson (1980) and the classical solution of Chwang & Wu (1975) for a prolate ellipsoid, the recent theory of Walker *et al.* (2020*a*) surpasses these general shortfalls and leverages a particular choice of kernel $\boldsymbol{K}^{\chi}$, along with a systematically justified and spatially dependent regularisation parameter χ, to satisfy the no-slip boundary condition on the surface of a slender body up to errors algebraic in the body aspect ratio. This theory retains the non-singular nature and accompanying

https://doi.org/10.1017/jfm.2021.139 Published online by Cambridge University Press

numerical simplicity of the general regularised ansatz, whilst expanding upon the scope of Johnson's work and affording systematically justified accuracy and parameterisation to a wide range of slender bodies. With such features having been absent from the recent efficient frameworks of Moreau *et al.* (2018), Hall-McNair *et al.* (2019) and Walker *et al.* (2019), the primary aim of this study is to incorporate the theory of Walker *et al.* (2020*a*) into the coarse-grained elastohydrodynamic framework of Walker *et al.* (2019), enabling the efficient simulation of slender bodies with asymptotically justified hydrodynamic accuracy in the no-slip condition. In doing so, we will additionally attempt to address concerning oscillations present in the force density solutions of these frameworks, which reportedly persist even with improved filament discretisations (Cortez 2018; Walker *et al.* 2019).

However, whilst the incorporation of the simple ansatz of Walker *et al.* (2020*a*) may be achieved with relative ease, integration of the regular but rapidly varying kernels may limit the speed of computation if performed with quadrature, as implemented in the original work of Walker *et al.* (2020*a*). Having built upon the works of Smith (2009) and Cortez (2018), respectively, Hall-McNair *et al.* (2019) and Walker *et al.* (2019) avoid such expensive computation by analytically integrating the kernel over the straight line segments that form the discretised centreline of the slender body, which we will refer to as the regularised Stokeslet segment (RSS) approach. Although complicated here by a non-constant regularisation parameter χ, we will aim to proceed in a similar fashion and remove the reliance on quadrature rules in order to realise a highly efficient numerical framework for the study of slender-body elastohydrodynamics.

Hence, we will proceed by first defining the non-uniform filament problem, adopting and unifying the notation of Walker *et al.* (2019, 2020*a*) for slender-body kinematics. We then describe a modification of the coarse-grained framework of Moreau *et al.* (2018), similar in form to that of Walker *et al.* (2019), and present the slender-body theory of Walker *et al.* (2020*a*) cast in dimensionless quantities. Having adopted a piecewise-constant discretisation of viscous force density, we then seek to perform the slender-body integrals analytically, Taylor expanding the regularisation parameter χ to yield symbolic tractability. We will then numerically evidence the improved satisfaction of the no-slip boundary condition on the surface of the filament attained with the presented methodology. In turn, we will then consider the computed profiles of force density along the centreline of the filament and their behaviour near the endpoints of the slender body.

2. The non-uniform filament problem

In this work, we will consider the planar motions of a thin inextensible, unshearable, untwistable filament in a viscous fluid, with the filament centreline denoted $\boldsymbol{x}(s,t) = x(s,t)\boldsymbol{e}_x + y(s,t)\boldsymbol{e}_y$, without loss of generality, where $\boldsymbol{e}_x, \boldsymbol{e}_y$ are constant orthogonal unit vectors in a fixed inertial reference frame and span the plane of motion. Here, $s \in [0, L]$ is an arclength parameter and time is denoted by t, where L is the length of the slender object. Distinct from the notation of the Introduction, this slenderness is captured by the dimensionless parameter ϵ, defined explicitly as

$$\epsilon = \frac{2\max_{s\in[0,L]}\{\eta(s)\}}{L} \ll 1, \tag{2.1}$$

where $\eta(s)$ is the non-negative radius of the filament at arclength s, having assumed local axisymmetry about the centreline. With the shape therefore entirely defined by the

https://doi.org/10.1017/jfm.2021.139 Published online by Cambridge University Press

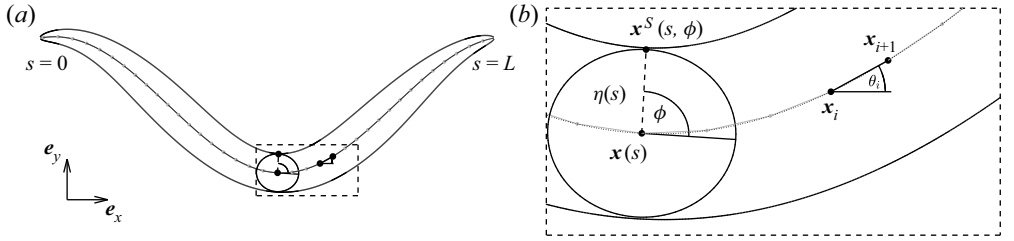


Figure 1. Filament set-up and notation. (*a*) A general locally axisymmetric filament of total length L, with its centreline contained in a plane spanned by $\boldsymbol{e}_x$ and $\boldsymbol{e}_y$. (*b*) A zoomed view of the slender body, with centreline $\boldsymbol{x}(s)$ and associated surface points $\boldsymbol{x}^S(s,\phi)$ parameterised by angle ϕ at a distance $\eta(s)$ from the centreline. Discrete points are shown as grey circles, connected by solid straight line segments that approximate the smooth dotted centreline. Example such discrete points $\boldsymbol{x}_i$ and $\boldsymbol{x}_{i+1}$ are highlighted in black, with the connecting line segment defining the angle θ_i relative to the fixed $\boldsymbol{e}_x$ direction.

centreline and radius function, we may describe points on the surface of the filament as

$$\boldsymbol{x}^S(s,\phi) = \boldsymbol{x}(s) + \eta(s)\boldsymbol{e}_r(s,\phi), \tag{2.2}$$

where ϕ is a cross-sectional angle. Here, $\boldsymbol{e}_r$ is a radial unit vector embedded in a transverse cross-section to the centreline. For unit tangent, normal and binormal unit vectors defined by the Frenet–Serret relations

$$\boldsymbol{e}_t(s) = \frac{\partial \boldsymbol{x}}{\partial s}, \quad \frac{\partial \boldsymbol{e}_t}{\partial s} = \theta_s \boldsymbol{e}_n(s), \quad \boldsymbol{e}_b(s) = \boldsymbol{e}_t(s) \times \boldsymbol{e}_n(s), \tag{2.3a–c}$$

where $\theta(s,t)$ defines the filament tangent angle relative to $\boldsymbol{e}_x$, we define

$$\boldsymbol{e}_r(s,\phi) = \boldsymbol{e}_n(s)\cos\phi + \boldsymbol{e}_b(s)\sin\phi. \tag{2.4}$$

Here, and throughout, subscripts of s denote derivatives with respect to arclength and we have omitted writing the inherent time dependence of the filament centreline and all derived quantities. These definitions are illustrated in figure 1.

We discretise the filament centreline into N linear segments, with the endpoints of these segments denoted by $\boldsymbol{x}(s_i)$ for uniformly spaced arclengths $s_i = (i-1)L/N \in [0, L]$, where $i = 1, \ldots, N+1$. We write $\boldsymbol{t}_i$ for the unit tangent to each linear segment, noting that this is an approximation of $\boldsymbol{e}_t(s)$ on the ith segment, and parameterise these discrete tangents by $\theta(s)$, itself discretised as $\theta(s) \approx \theta_i$ on the ith segment such that $\boldsymbol{t}_i = \cos\theta_i \boldsymbol{e}_x + \sin\theta_i \boldsymbol{e}_y$. With this piecewise-linear discretisation of $\boldsymbol{x}$ in arclength, or equivalently a piecewise-constant discretisation of θ, we may describe the position of the filament with only the $N+2$ quantities $x_1, y_1, \theta_1, \ldots, \theta_N$, where $\boldsymbol{x}_1 = x_1\boldsymbol{e}_x + y_1\boldsymbol{e}_y$. Explicitly, for $j = 1, \ldots, N+1$ we have

$$\boldsymbol{x}_j = \boldsymbol{x}_1 + \sum_{i=1}^{j-1} (\cos\theta_i \boldsymbol{e}_x + \sin\theta_i \boldsymbol{e}_y)\Delta s, \tag{2.5}$$

where Δs is the constant segment length, equivalently defined as $\Delta s = L/N$. Differentiating with respect to time, denoting time derivatives with a dot, this gives the

https://doi.org/10.1017/jfm.2021.139 Published online by Cambridge University Press

linear velocity of the material point $\boldsymbol{x}_j$ as

$$\dot{\boldsymbol{x}}_j = \dot{\boldsymbol{x}}_1 + \sum_{i=1}^{j-1} (-\sin\theta_i \boldsymbol{e}_x + \cos\theta_i \boldsymbol{e}_y)\dot{\theta}_i \Delta s. \tag{2.6}$$

We may concisely write this latter linear relation as

$$\boldsymbol{Q}\dot{\boldsymbol{\theta}} = \dot{\boldsymbol{X}}, \tag{2.7}$$

where $\boldsymbol{\theta} = [x_1, y_1, \theta_1, \ldots, \theta_N]^{\mathrm{T}}$, $\boldsymbol{X} = [x_1, y_1, \ldots, x_{N+1}, y_{N+1}]^{\mathrm{T}}$ and $\boldsymbol{Q}$ is the linear operator encoding (2.6), the latter having dimension $(2N+2) \times (N+2)$ and given explicitly in the work of Walker *et al.* (2019). Hence, we may readily cast expressions involving $\dot{\boldsymbol{X}}$ in terms of the reduced variables $\boldsymbol{\theta}$ and their time derivatives.

The equations governing the surrounding fluid medium will be the familiar Newtonian Stokes equations, valid in the inertia-free limit of zero Reynolds number, which we will assume throughout. This limit is relevant to a broad range of biological and physical circumstances, for example the small-scale beating of spermatozoan flagella or the bending of cilia in flow. The Stokes equations may be briefly stated as

$$\mu \nabla^2 \boldsymbol{u} = \nabla p, \quad \nabla \cdot \boldsymbol{u} = 0, \tag{2.8a,b}$$

where $\boldsymbol{u}$ is the fluid velocity, μ is the associated viscosity and p is the pressure. Here, we will also assume that the flow is in an unbounded domain in the exterior of the filament, and decays to zero in the far field.

3. No-slip elastohydrodynamics

3.1. *Coarse-grained mechanics*

We follow Moreau *et al.* (2018), stating the governing equations of elasticity for this slender inextensible unshearable filament in pointwise form as

$$\boldsymbol{n}_s - \boldsymbol{f} = \boldsymbol{0}, \tag{3.1}$$

$$\boldsymbol{m}_s + \boldsymbol{x}_s \times \boldsymbol{n} = \boldsymbol{0}, \tag{3.2}$$

for contact force and couple denoted $\boldsymbol{n}$ and $\boldsymbol{m}$, respectively, and where a subscript of s denotes differentiation with respect to arclength. Here, and throughout, the filament is passive, with no driving internal couple, and $\boldsymbol{f}$ denotes the force per unit length applied on the surrounding fluid by the filament. Note that the external couple exerted by the fluid on the filament is $O(\epsilon^2)$, which will be negligible at the level of asymptotic approximation that we will consider in this work. To proceed, we integrate these equations with respect to arclength s, yielding

$$-\sum_{j=1}^{N} \int_{s_j}^{s_{j+1}} \boldsymbol{f}(s)\,\mathrm{d}s = \boldsymbol{n}(0), \tag{3.3}$$

$$-\sum_{j=i}^{N} \int_{s_j}^{s_{j+1}} (\boldsymbol{x}(s) - \boldsymbol{x}_i) \times \boldsymbol{f}(s)\,\mathrm{d}s = \boldsymbol{m}(s_i), \quad i = 1, \ldots, N, \tag{3.4}$$

where we have decomposed the integrals into those over discrete segments and integrated the pointwise moment balance from $s = s_i$ to $s = s_{N+1} = L$ for $i = 1, \ldots, N$. In writing

https://doi.org/10.1017/jfm.2021.139 Published online by Cambridge University Press

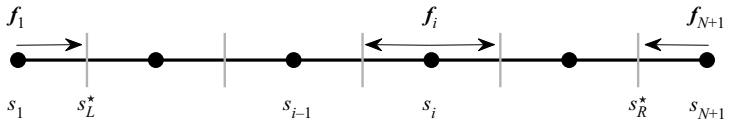


Figure 2. Illustration of the piecewise-constant force density discretisation. The horizontal line represents arclength s, with the discrete arclengths s_i corresponding to segment endpoints shown as black circles. The force density $\boldsymbol{f}$ is approximated as taking the value $\boldsymbol{f}_i$ in a neighbourhood of the arclength s_i, typically between the midpoints $(s_{i-1}+s_i)/2$ and $(s_i+s_{i+1})/2$ of the adjacent segments, which are shown as vertical grey lines. The exceptional cases are on the first and final segments, where the midpoints are replaced with $s_L^\star$ and $s_R^\star$, respectively, in order to simplify the later description of the hydrodynamic slender-body theory.

(3.3) and (3.4), we have assumed that the filament is force and moment free at $s = L$, equivalent to imposing $\boldsymbol{n}(L) = \boldsymbol{m}(L) = \boldsymbol{0}$. We additionally assume that these conditions hold at the base, so that $\boldsymbol{n}(0) = \boldsymbol{m}(0) = \boldsymbol{0}$, although each of these boundary conditions may be readily replaced with those appropriate for particular problem settings, for example the clamping of one end of the filament. Recalling that the considered filament motion is purely planar, each term of (3.4) is proportional to $\boldsymbol{e}_x \times \boldsymbol{e}_y = \boldsymbol{e}_z$, with $\boldsymbol{m}(s_i) = m(s_i)\boldsymbol{e}_z$, so that (3.4) collapses onto N scalar equations. We adopt a simple constitutive law, writing $\boldsymbol{m}(s_i) = EI\theta_s(s_i) \approx EI(\theta_i - \theta_{i-1})/\Delta s$ for bending stiffness EI, valid for $i = 2, \ldots, N$.

Illustrated in figure 2, we discretise the force density $\boldsymbol{f}$, adopting a piecewise-constant representation that is distinct from that of θ. Denoting the value taken by $\boldsymbol{f}$ at the segment endpoints $\boldsymbol{x}_i$ by $\boldsymbol{f}_i$, for $i = 1, \ldots, N+1$, we discretise $\boldsymbol{f}$ as

$$\boldsymbol{f}(s) = \begin{cases} \boldsymbol{f}_i, & s \in \left[s_i, s_i + \dfrac{\Delta s}{2}\right) \\ \boldsymbol{f}_{i+1}, & s \in \left[s_i + \dfrac{\Delta s}{2}, s_{i+1}\right), \end{cases} \tag{3.5}$$

where $i \in \{2, \ldots, N-1\}$ is such that $s \in [s_i, s_{i+1})$. This is equivalent to stating that, on segments $i = 2, \ldots, N-1$, the value taken by $\boldsymbol{f}$ is equal to that at the closest segment endpoint, with the ith segment effectively split into two halves. The definition on the first and last segments is similar, although the segment is not precisely split into two equal parts, which will enable a concise description of the slender-body theory in § 3.2. Defining $e = \sqrt{1-\epsilon^2}$ to be the effective filament eccentricity, on the first segment we take

$$\boldsymbol{f}(s) = \begin{cases} \boldsymbol{f}_1, & s \in [s_1, s_L^\star) \\ \boldsymbol{f}_2, & s \in [s_L^\star, s_2) \end{cases} \quad \text{for } s_L^\star = \frac{1}{2}\left(\frac{L(1-e)}{2} + \Delta s\right), \tag{3.6}$$

whilst on the last segment we analogously have

$$\boldsymbol{f}(s) = \begin{cases} \boldsymbol{f}_N, & s \in [s_N, s_R^\star) \\ \boldsymbol{f}_{N+1}, & s \in [s_R^\star, s_{N+1}) \end{cases} \quad \text{for } s_R^\star = \frac{1}{2}\left(\frac{L(3+e)}{2} - \Delta s\right). \tag{3.7}$$

Whilst this is somewhat cumbersome, with the first and last segments being treated differently to the others, we have found that it yields significant advantages over simpler piecewise-constant and linear schemes found in the literature. In particular, attempts at a piecewise-linear approximation, as in Walker *et al.* (2019), result in large endpoint oscillations in the computed values of $\boldsymbol{f}$, akin to those found in the RSS methodology of Cortez (2018) and are examined further in § 4.3.2, where we evidence a lack of such oscillations in the approach presented in this study. A natural alternative, in which $\boldsymbol{f}$ is

https://doi.org/10.1017/jfm.2021.139 Published online by Cambridge University Press

constant on each segment, yields equivalently undesirable results, with the methodology becoming numerically intractable due to stiffness when considering nearly straight filaments. Indeed, the same issue is present in the scheme proposed by Hall-McNair *et al.* (2019), which utilises this intuitive discretisation. Though these issues are circumvented by the approach presented in this work, the source of this sensitive numerical dependence of the filament problem on discretisation remains unclear, and warrants future investigation.

Returning to the now-discretised filament problem, the force density dependence of (3.3) and (3.4) may be cast as a simple linear operator, denoted by $\boldsymbol{B}$, allowing us to write

$$-\boldsymbol{B}\boldsymbol{F} = \boldsymbol{R}, \tag{3.8}$$

where $\boldsymbol{R} = [0, 0, m(s_1), \ldots, m(s_N)]^{\mathrm{T}}$ encodes the bending moments and total force acting on the filament, whilst $\boldsymbol{F} = [\boldsymbol{f}_1 \cdot \boldsymbol{e}_x, \boldsymbol{f}_1 \cdot \boldsymbol{e}_y, \ldots, \boldsymbol{f}_{N+1} \cdot \boldsymbol{e}_x, \boldsymbol{f}_{N+1} \cdot \boldsymbol{e}_y]^{\mathrm{T}}$ is the vector of discretised force densities. The first two rows $\boldsymbol{B}_1, \boldsymbol{B}_2$ of $\boldsymbol{B}$ represent total force balance over the filament, and are given explicitly by

$$\boldsymbol{B}_1 = \frac{\Delta s}{2}[1 + d, 0, 2 - d, 0, 2, 0, \ldots, 2, 0, 2 - d, 0, 1 + d, 0], \tag{3.9}$$

$$\boldsymbol{B}_2 = \frac{\Delta s}{2}[0, 1 + d, 0, 2 - d, 0, 2, 0, \ldots, 2, 0, 2 - d, 0, 1 + d], \tag{3.10}$$

where $d = L(1 - e)/(2\Delta s)$. The remaining rows $\boldsymbol{B}_{i+2}$ encode the integrated moment balance equations for $i = 1, \ldots, N$, the expressions for which are given in Appendix A.

We now suppose that an invertible linear operator $\boldsymbol{A}$ may be constructed such that

$$\dot{\boldsymbol{X}} = \boldsymbol{A}\boldsymbol{F}(1 + O(\epsilon)), \tag{3.11}$$

which we will find explicitly in § 3.2. Upon substitution of (3.11) into (3.8), also making use of (2.7), we obtain the leading-order coarse-grained linear system

$$-\boldsymbol{B}\boldsymbol{A}^{-1}\boldsymbol{Q}\dot{\boldsymbol{\theta}} = \boldsymbol{R}, \tag{3.12}$$

where $\boldsymbol{B}$ encodes the integrated equations of elasticity, $\boldsymbol{A}$ represents the hydrodynamic relation between velocity and force density, $\boldsymbol{Q}$ links the kinematic descriptions of the filament and $\boldsymbol{R}$ is the elastic response of the filament to bending.

Finally, we non-dimensionalise lengths by filament half-length $L/2$, forces with $4EI/L^2$ and time with some characteristic time scale T. This yields the dimensionless system

$$-E_h\hat{\boldsymbol{B}}\hat{\boldsymbol{A}}^{-1}\hat{\boldsymbol{Q}}\dot{\hat{\boldsymbol{\theta}}} = \hat{\boldsymbol{R}}, \quad E_h = \frac{\pi\mu L^4}{2EIT}, \tag{3.13a,b}$$

where the notation $\hat{\cdot}$ denotes dimensionless quantities, and we note that the rescaled arclength parameter is $\hat{s} = 2s/L \in [0, 2]$. The elastohydrodynamic number E_h here is analogous to that of Walker *et al.* (2019), although it differs by a factor of 16 due to differing choices of length scale. We have the explicit relations

$$\boldsymbol{B} = \frac{L^2}{4}\hat{\boldsymbol{B}}, \quad \boldsymbol{A} = \frac{1}{8\pi\mu}\hat{\boldsymbol{A}}, \quad \boldsymbol{Q}\dot{\boldsymbol{\theta}} = \frac{L}{2T}\hat{\boldsymbol{Q}}\dot{\hat{\boldsymbol{\theta}}}, \quad \boldsymbol{R} = \frac{2EI}{L}\hat{\boldsymbol{R}}, \tag{3.14a–d}$$

between dimensional and dimensionless quantities, having multiplied the force balance equations by $\Delta s/2$ and absorbed the dimensional scalings of x_1, y_1 into $\boldsymbol{Q}$ for convenience,

https://doi.org/10.1017/jfm.2021.139 Published online by Cambridge University Press

writing $\hat{\boldsymbol{\theta}} = (\hat{x}_1, \hat{y}_1, \theta_1, \ldots, \theta_N)^{\mathrm{T}}$. In what follows, we will drop the $\hat{\cdot}$ notation for dimensionless variables, although for later convenience we first write

$$\eta(s) = \frac{L}{2}\hat{\eta}(\hat{s}) = \frac{\epsilon L}{2}\tilde{\eta}(\hat{s}) \tag{3.15}$$

and immediately drop the tilde on $\tilde{\eta}(\hat{s}) \sim O(1)$. For clarity, the points on the surface of the filament may now be written in terms of dimensionless quantities as

$$\boldsymbol{x}^S(s, \phi) = \boldsymbol{x}(s) + \epsilon\eta(s)\boldsymbol{e}_r(s, \phi). \tag{3.16}$$

3.2. *Non-uniform hydrodynamics*

Before describing the slender-body theory of Walker *et al.* (2020*a*) that we will use to relate forces and flow, we first recapitulate the well-known regularised singularities of Cortez (2001) and Ainley *et al.* (2008) on which it is built. Following Walker *et al.* (2020*a*), for points $\boldsymbol{\alpha}$, $\boldsymbol{\beta}$ and the particular choices of mollifier given in Appendix B, the regularised Stokeslet $\boldsymbol{S}^\chi$ and potential dipole $\boldsymbol{D}^\chi$ are given by

$$\boldsymbol{S}^\chi(\boldsymbol{\alpha}, \boldsymbol{\beta}) = \frac{(|\boldsymbol{\alpha} - \boldsymbol{\beta}|^2 + 2\chi)\boldsymbol{I}}{(|\boldsymbol{\alpha} - \boldsymbol{\beta}|^2 + \chi)^{3/2}} + \frac{\boldsymbol{T}(\boldsymbol{\alpha}, \boldsymbol{\beta})}{(|\boldsymbol{\alpha} - \boldsymbol{\beta}|^2 + \chi)^{3/2}}, \tag{3.17}$$

$$\boldsymbol{D}^\chi(\boldsymbol{\alpha}, \boldsymbol{\beta}) = -\frac{(|\boldsymbol{\alpha} - \boldsymbol{\beta}|^2 - 2\chi)\boldsymbol{I}}{(|\boldsymbol{\alpha} - \boldsymbol{\beta}|^2 + \chi)^{5/2}} + \frac{3\boldsymbol{T}(\boldsymbol{\alpha}, \boldsymbol{\beta})}{(|\boldsymbol{\alpha} - \boldsymbol{\beta}|^2 + \chi)^{5/2}}, \tag{3.18}$$

where $\boldsymbol{T}(\boldsymbol{\alpha}, \boldsymbol{\beta}) = (\boldsymbol{\alpha} - \boldsymbol{\beta}) \otimes (\boldsymbol{\alpha} - \boldsymbol{\beta})$, $\boldsymbol{I}$ is the 3×3 identity tensor and χ is the regularisation parameter.

Throughout this section, it will be convenient to consider functions of filament arclength instead as functions of a shifted arclength parameter $s' \in [-1, 1]$, which will greatly simplify the notation associated with the slender-body theory of Walker *et al.* (2020*a*). We will consistently abuse notation and write $\boldsymbol{x}(s) \equiv \boldsymbol{x}(s')$, where $s = s' + 1$ and other functions of arclength are treated analogously. In particular, this enables us to concisely define the arclength-dependent regularisation parameter $\chi = \chi(s')$, which may be written as

$$\chi(s') = \epsilon^2[(1 - s'^2) - \eta^2(s')]. \tag{3.19}$$

This choice of regularisation parameter ensures a convenient form of the regularised Stokeslet and potential dipole when evaluated on the surface of the slender body, as discussed in detail in the work of Walker *et al.* (2020*a*). The analysis of Walker *et al.* (2020*a*) imposed a restriction on the derivative of $\chi(s')$, requiring $\mathrm{d}\chi(s')/\mathrm{d}s' = O(\epsilon^2)$ in order to Taylor expand $\chi(s')$ with sufficiently small error in an inner region. However, we remark that this may in fact be relaxed to a Lipschitz condition on $\chi(s')$, with differentiability of $\chi(s')$ no longer required by the slender theory. Precisely, the error analysis of Walker *et al.* (2020*a*, (3.21)) still holds if $\chi(s')$ satisfies a Lipschitz condition with constant $L_\chi = O(\epsilon^2)$, which in turn is satisfied if $\eta^2(s')$ is Lipschitz with an $O(1)$ constant. This serves to explain the numerical explorations of Walker *et al.*, in which the consideration of non-differentiable $\chi(s')$ was noted to not result in large errors in the slender theory, despite the violation of differentiability assumptions.

Returning to our hydrodynamic formulation and recalling the effective filament eccentricity as $e = \sqrt{1 - \epsilon^2}$, the dimensionless ansatz of Walker *et al.* (2020*a*) for the

https://doi.org/10.1017/jfm.2021.139 Published online by Cambridge University Press

fluid velocity at a point $\boldsymbol{y}$ in terms of the force per unit length $\boldsymbol{f}(s')$ may now be written as

$$\boldsymbol{u}(\boldsymbol{y}) = \int_{-e}^{e} \left[\boldsymbol{S}^{\chi(s')}(\boldsymbol{y}, \boldsymbol{x}(s')) - \frac{1-e^2}{2e^2}(e^2 - s'^2)\boldsymbol{D}^{\chi(s')}(\boldsymbol{y}, \boldsymbol{x}(s')) \right] \boldsymbol{f}(s')\,\mathrm{d}s', \tag{3.20}$$

noting that the dimensional factor of $8\pi\mu$ has been absorbed by the scalings of (3.14*a–d*). Note that the limits in the integral are between $-e$ and e, rather than -1 and 1, as inherited ultimately from the Chwang & Wu solution for a translating prolate ellipsoid, as detailed in Walker *et al.* (2020*a*). Taking $\boldsymbol{y} = \boldsymbol{x}^S(s_i', \phi)$, where $s_i' = s_i - 1$ are the shifted dimensionless arclengths corresponding to the discrete points s_i, we may apply this ansatz at the filament surface to generate the $N+1$ vector equations

$$\begin{aligned}\boldsymbol{u}(\boldsymbol{x}^S(s_i', \phi)) = \int_{-e}^{e} \Bigg[& \boldsymbol{S}^{\chi(s')}(\boldsymbol{x}^S(s_i', \phi), \boldsymbol{x}(s')) \\ & - \frac{1-e^2}{2e^2}(e^2 - s'^2)\boldsymbol{D}^{\chi(s')}(\boldsymbol{x}^S(s_i', \phi), \boldsymbol{x}(s')) \Bigg] \boldsymbol{f}(s')\,\mathrm{d}s'. \end{aligned} \tag{3.21}$$

We impose the no-slip condition $\boldsymbol{u}(\boldsymbol{x}^S(s_i', \phi)) = \dot{\boldsymbol{x}}^S(s', \phi)$ on the surface of the filament, and may decompose

$$\dot{\boldsymbol{x}}^S(s', \phi) = \dot{\boldsymbol{x}}(s') + \epsilon\boldsymbol{\omega}(s')\eta(s') \times \boldsymbol{e}_r(s', \phi), \tag{3.22}$$

for centreline velocity $\dot{\boldsymbol{x}}(s')$ and angular velocity $\boldsymbol{\omega}(s')$ measured about $\boldsymbol{x}(s')$, recalling that the filament is assumed to be unshearable. Supposing that $\boldsymbol{\omega}$ is $O(1)$ as $\epsilon \to 0$, consistent with the filament being assumed untwistable and planar, at leading order we simply have

$$\dot{\boldsymbol{x}}^S(s', \phi) = \dot{\boldsymbol{x}}(s') + O(\epsilon), \tag{3.23}$$

independent of ϕ. Finally, we arrive at the leading-order relation

$$\begin{aligned}\dot{\boldsymbol{x}}(s_i') \approx \int_{-e}^{e} \Bigg[& \boldsymbol{S}^{\chi(s')}(\boldsymbol{x}^S(s_i', \phi), \boldsymbol{x}(s')) \\ & - \frac{1-e^2}{2e^2}(e^2 - s'^2)\boldsymbol{D}^{\chi(s')}(\boldsymbol{x}^S(s_i', \phi), \boldsymbol{x}(s')) \Bigg] \boldsymbol{f}(s')\,\mathrm{d}s'. \end{aligned} \tag{3.24}$$

For comparison, the equivalent expression used in the method of regularised Stokeslet segments, and indeed many regularised slender-body theories (Gillies *et al.* 2009; Cortez & Nicholas 2012; Olson *et al.* 2013), may be written as

$$\dot{\boldsymbol{x}}(s_i') \approx \int_{-1}^{1} \boldsymbol{S}^{\epsilon^2/4}(\boldsymbol{x}(s_i'), \boldsymbol{x}(s'))\boldsymbol{f}(s')\,\mathrm{d}s', \tag{3.25}$$

where we note in particular that the evaluations of the regularised Stokeslet kernel are on the filament centreline, not on the surface of the slender body.

Although the left-hand side of (3.24) is trivially independent of the cross-sectional angle ϕ, it is not clear if the integral is similarly independent. However, with the particular choice of regularisation parameter $\chi(s')$ given in (3.19), Walker *et al.* (2020*a*) showed

https://doi.org/10.1017/jfm.2021.139 Published online by Cambridge University Press

that the integral of (3.21) is in fact independent of ϕ at leading order in ϵ, with errors linear in the aspect ratio. Thus, (3.24) satisfies this necessary condition. Moreover, its solution enables the no-slip condition on the surface of the filament to be satisfied to $O(\epsilon)$. With the force density $\boldsymbol{f}$ discretised as described in § 3.1 and incurring errors proportional to $\Delta s\, \|\mathrm{d}\boldsymbol{f}/\mathrm{d}s\|$, which are assumed small and may be verified *a posteriori*, yields the leading-order linear system

$$\dot{X} = \boldsymbol{A}\boldsymbol{F} \tag{3.26}$$

relating force densities on the filament to the centreline velocities.

3.3. *Regularised non-uniform segments*

The entries of $\boldsymbol{A}$ may be readily computed with quadrature, as was performed in the original work of Walker *et al.* (2020*a*). However, with the integral kernels rapidly varying in some regions, this can be prohibitively expensive in elastohydrodynamic simulations, where numerous evaluations of $\boldsymbol{A}$ are typically required. Inspired by the recent method of regularised Stokeslet segments, as detailed by Cortez (2018) and used in the work of Walker *et al.* (2019), we seek to evaluate these integrals analytically on each linear segment of the filament, in general incurring discretisation errors as a result of the arclength-dependent regularisation $\chi(s')$. We will refer to this approach as the method of regularised non-uniform segments (RNS).

With $\boldsymbol{f}$ approximated as piecewise constant, computation of $\boldsymbol{A}$ reduces to performing a number of integrals over the discrete straight segments of the filament. We consider such an integral over the jth segment, parameterised by $\alpha \in [0, 1]$, on which we write $\chi = \chi(\alpha)$ and the filament centreline is given by $\boldsymbol{x}(\alpha) = \boldsymbol{x}_j - \alpha\boldsymbol{v}$, where $\boldsymbol{v} = \boldsymbol{x}_j - \boldsymbol{x}_{j+1}$. This formulation is applicable even to the first and last segments, subject to the substitution of $\boldsymbol{x}_1$ by $\boldsymbol{x}(-e)$ and of $\boldsymbol{x}_{N+1}$ by $\boldsymbol{x}(e)$, owing to the chosen discretisation of $\boldsymbol{f}$. With this discretised $\boldsymbol{f}$ taking the values $\boldsymbol{f}_j$ and $\boldsymbol{f}_{j+1}$ on different halves of this segment, we require expressions for the integrals evaluated on two subdomains, $\alpha \in [0, 1/2]$ and $\alpha \in [1/2, 1]$. Further, analogous to Cortez (2018) and Walker *et al.* (2019) and given explicitly in Appendix C, we note that this discretisation of $\boldsymbol{f}$ has rendered each of these integrals as linear combinations of

$$T^L_{m,q} = \int_0^{1/2} \alpha^m R^q \,\mathrm{d}\alpha, \quad T^R_{m,q} = \int_{1/2}^{1} \alpha^m R^q \,\mathrm{d}\alpha, \tag{3.27a,b}$$

where we define $R = \left(\left|\boldsymbol{x}_i^S - \boldsymbol{x}_j + \alpha\boldsymbol{v}\right|^2 + \chi(\alpha)\right)^{1/2}$ for a surface point $\boldsymbol{x}_i^S = \boldsymbol{x}^S(s_i', \phi)$, with ϕ arbitrary, as above. These integrals may be readily performed in the case that R^2 is a quadratic function of α, as in the original method of regularised Stokeslet segments although here prohibited in general by $\chi(\alpha)$.

In order to recover this desirable property, we Taylor expand $\chi(\alpha)$ about an endpoint of the segment, either $\alpha = 0$ or $\alpha = 1$, assuming sufficient smoothness of χ. The expansion point is chosen in order to minimise the error in the resulting integral, noting in particular that $R(\alpha)$ can become $O(\epsilon)$ if $\boldsymbol{x}_j - \alpha\boldsymbol{v}$ nears $\boldsymbol{x}_i^S$, for example in the trivial case of $i = j$. With χ therefore plausibly the dominant term in this $O(\epsilon)$ neighbourhood, we choose to expand $\chi(\alpha)$ about the segment endpoint that is closest to $\boldsymbol{x}_i^S$, denoting the value of α at this endpoint as $\alpha^\star$. Collecting powers of α, in each case this yields an expansion of the

https://doi.org/10.1017/jfm.2021.139 Published online by Cambridge University Press

form

$$R(\alpha)^2 = A + B\alpha + C\alpha^2 + E, \quad |E| \leqslant \begin{cases} \dfrac{1}{6}\alpha^3 \, |\boldsymbol{v}|^3 \sup \left| \dfrac{\mathrm{d}^3\chi}{\mathrm{d}s'^3} \right|, & \alpha^\star = 0, \\ \dfrac{1}{6}(1-\alpha)^3 \, |\boldsymbol{v}|^3 \sup \left| \dfrac{\mathrm{d}^3\chi}{\mathrm{d}s'^3} \right|, & \alpha^\star = 1. \end{cases} \tag{3.28a,b}$$

In the error term E we have bounded the third derivative of χ over the segment, and have cast the derivative in terms of the normalised arclength s' in order to unify our phrasing of model assumptions. With $R(\alpha) = O(\epsilon)$ when $\left|\boldsymbol{x}_i^S - \boldsymbol{x}_j + \alpha\boldsymbol{v}\right| = O(\epsilon)$, and $R(\alpha)$ strictly order unity otherwise, when $\alpha^\star = 0$ this error term is subdominant if

$$\frac{1}{6}\alpha^3 \Delta\mathrm{s}^3 \sup \left| \frac{\mathrm{d}^3\chi}{\mathrm{d}s'^3} \right| = \begin{cases} O(\epsilon^3), & \text{where } \left|\boldsymbol{x}_i^S - \boldsymbol{x}_j + \alpha\boldsymbol{v}\right| = O(\epsilon), \\ O(\epsilon), & \text{otherwise}, \end{cases} \tag{3.29}$$

noting that $|\boldsymbol{v}| \leqslant \Delta\mathrm{s}$, with a similar expression required for $\alpha^\star = 1$. This imposes a weak restriction on the derivatives of χ and the discretisation length $\Delta\mathrm{s}$, recalling that $\chi = O(\epsilon^2)$ everywhere, although we remark that these differentiability assumptions may be relaxed if a sufficiently accurate quadratic approximation to $\chi(s')$ was nevertheless available. Recalling (3.19), these assumptions translate into similar conditions on $\eta^2(s')$, the square of the radius function. We proceed assuming that the differentiability restrictions of (3.29) hold, whereupon we drop the error term E in what follows, approximating $R(\alpha)^2$ as a quadratic function on each segment. The segment-dependent coefficients A, B, C may be readily computed when expanding with $\alpha^\star = 0$ or $\alpha^\star = 1$, and for $\alpha^\star = 0$ are given explicitly by

$$A = |\boldsymbol{x}_i^S - \boldsymbol{x}_j|^2 + \chi, \quad B = 2\boldsymbol{v} \cdot (\boldsymbol{x}_i^S - \boldsymbol{x}_j) + |\boldsymbol{v}| \frac{\mathrm{d}\chi}{\mathrm{d}s'}, \quad C = |\boldsymbol{v}|^2 \left(1 + \frac{1}{2}\frac{\mathrm{d}^2\chi}{\mathrm{d}s'^2}\right), \tag{3.30a–c}$$

where evaluations of χ and its derivatives for A, B, C are at $\alpha = 0$ and we henceforth write $R(\alpha)^2 = A + B\alpha + C\alpha^2$ for brevity. Omitted here for brevity, analogous expressions hold for A, B, C when $\alpha^\star = 1$. As noted above and written explicitly in Appendix C, the integral kernel may be decomposed into a linear combination of terms $\alpha^m R^q$ for $(m, q) \in \{(0,-1), (0,-3), (0,-5), (1,-3), (1,-5), (2,-3), (2,-5), (3,-5), (4,-5)\}$. For $m > 0$, computation of these quantities may be performed simply via the recurrence relations

$$T^L_{m+1,q-2} = \left.\frac{\alpha^m R^q}{qC}\right|_0^{1/2} - \frac{m}{qC} T^L_{m-1,q} - \frac{B}{2C} T^L_{m,q-2}, \tag{3.31}$$

$$T^R_{m+1,q-2} = \left.\frac{\alpha^m R^q}{qC}\right|_{1/2}^{1} - \frac{m}{qC} T^R_{m-1,q} - \frac{B}{2C} T^R_{m,q-2}, \tag{3.32}$$

where $q, C \neq 0$. These are analogous to the recurrence of Cortez (2018) and are similarly derived via integration by parts. Thus, explicit calculation of $T^L_{m,q}$ and $T^R_{m,q}$ is required only for $m = 0$, with the relevant antiderivatives given in Appendix D.

Hence, the construction of the operator $\boldsymbol{A}$ proceeds simply and efficiently: the coefficients A, B, C are evaluated from precomputed values of χ and its derivatives, the integrals $T^L_{m,q}, T^R_{m,q}$ are computed for $m = 0$ using the given antiderivatives, further

https://doi.org/10.1017/jfm.2021.139 Published online by Cambridge University Press

integrals for $m > 0$ are computed via the recurrences of (3.31) and (3.32), and the entries of $\boldsymbol{A}$ are formed as linear combinations of these terms following Appendix C. We additionally note that this process may be readily generalised to evaluation points that do not lie on the surface of the filament, in this case Taylor expanding about the segment endpoint that is closest to the evaluation point.

4. Verification and examples

4.1. *Efficiency and accuracy against quadrature*

Construction of the operator $\boldsymbol{A}$ via the method of regularised non-uniform segments introduces local approximations of the regularisation parameter χ wherever it is not simply a quadratic function of arclength, enabling analytic integration. We now compare this approach with quadrature in terms of both accuracy and efficiency in a practical parameter regime, considering three dimensionless radius functions $\eta(s')$ of varying complexity

$$\begin{aligned} &\text{(a)} \quad \sqrt{1-s'^2}, \\ &\text{(b)} \quad \sqrt{1-s'^2}(1-0.1\cos 2\pi s'), \\ &\text{(c)} \quad \sqrt{1-s'^2}(1.1+\sin 9\pi s'), \end{aligned} \tag{4.1}$$

each subject to normalisation and shown in figure 3. Considering a filament with a curved centreline, corresponding to the initial condition of figure 4(*a*), with $N = 100$ and $\epsilon = 0.02$ we compute $\boldsymbol{A}$ using both the RNS methodology and the inbuilt quadv routine in MATLAB®, with the numerical quadrature set to a tolerance of 10^{-12} and denoting the results of these computations by $\boldsymbol{A}_{RNS}$ and $\boldsymbol{A}_{Q}$, respectively. We write $\mathcal{E}$ for the relative matrix infinity norm error between these two results, defined explicitly as

$$\mathcal{E} = \frac{\left\| \boldsymbol{A}_{RNS} - \boldsymbol{A}_{Q} \right\|_{\infty}}{\left\| \boldsymbol{A}_{Q} \right\|_{\infty}}. \tag{4.2}$$

These relative errors are shown in figure 3, each of which can be seen to be several orders of magnitude lower than the asymptotic slenderness parameter. The rapidly varying curvature of case (c) gives rise to the largest error, consistent with the restrictions imposed on the derivatives of χ in (3.29), with the derivatives of χ in case (c) being orders of magnitude greater than in cases (a) and (b). Computations were performed on modest hardware (Intel® Core™ i7-6920HQ CPU), with the wall time for the RNS method being over two orders of magnitude less than that of the quadrature implementation, representing a significant improvement in computational efficiency for minimal reduction in accuracy. These observations of efficiency and accuracy hold for a range of considered body centrelines and radius functions, and are robust to variations in the slenderness parameter ϵ.

4.2. *Invariants of free-filament motion*

The coarse-grained framework for filament elasticity is similar to that presented and derived in the recent work of Walker *et al.* (2019), where it was extensively verified and benchmarked, utilising the stiff solver ode15s provided in MATLAB® with relative and absolute tolerances of 10^{-6} (Shampine & Reichelt 1997). However, due to the modification of considering a piecewise-constant discretisation of the force density $\boldsymbol{f}$, akin to the study of Moreau *et al.* (2018), we additionally verify the presented methodology in the case of a relaxing symmetric filament. Having taken $N = 40$ and $\epsilon = 0.02$, in figure 4

https://doi.org/10.1017/jfm.2021.139 Published online by Cambridge University Press

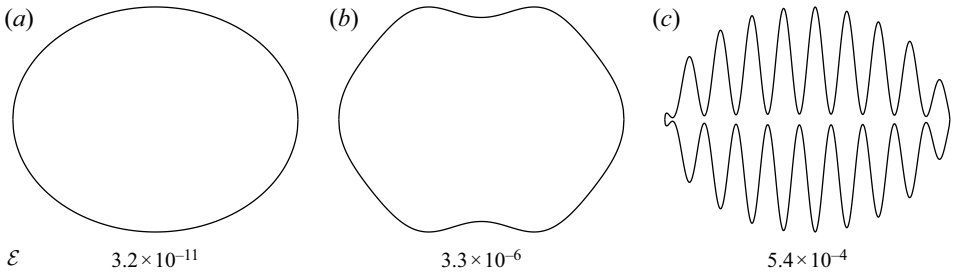


Figure 3. Example radius functions and the relative error $\mathcal{E}$ of using the RNS method in constructing the operator $\boldsymbol{A}$ compared with a quadrature rule of tolerance 10^{-12}. In each of the three cases, we note a small matrix infinity norm error $\mathcal{E}$, largest in case (c) where curvature of the radius function is rapidly varying. Here we have considered a curved filament in a dimensionless framework with $N = 100$ segments, having taken $\epsilon = 0.02$ and radius functions corresponding to (4.1). The filament centreline corresponds to the initial condition of figure 4(*a*), and shapes are shown stretched vertically for visual clarity.

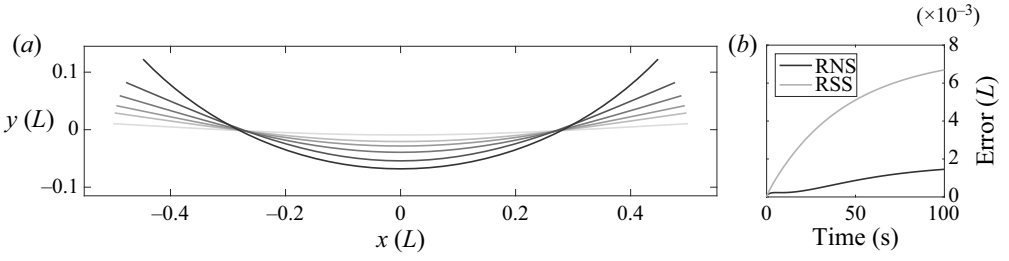


Figure 4. The relaxation of a symmetric filament, simulated with $N = 40$ segments for $E_h = 9600$. (*a*) Relaxation dynamics qualitatively matches that of Walker *et al.* (2019), in agreement with intuition and preserving the symmetry of the initial condition. (*b*) Distance translated by the centre of mass of the filament, as computed by the presented RNS methodology and the RSS approach of Walker *et al.* (2019), analytically zero and captured approximately here, having taken $N = 40$ and $\epsilon = 0.02$. Here, we have considered a filament with dimensionless shape $\eta(s') = \sqrt{1 - s'^2}$, corresponding to a prolate ellipsoid, although note that this information is not captured by the typical slender-body ansatz, as implemented in Walker *et al.* (2019).

we showcase the simulated dynamics of an initially symmetric filament relaxing to a straight configuration, during which we see that symmetry is preserved. Owing to the filament having no net force or torque act upon it, the centre of mass should not deviate from its initial position. Computing the translation of the centre of mass over the motion, a quantitative measure of framework accuracy, in figure 4(*b*) we see that this approximate constancy is preserved numerically with errors of the order of $10^{-3}L$, improved by an order of magnitude when compared to the previous methodology of Walker *et al.* (2019).

4.3. *Comparison against existing theories*

We now more thoroughly compare and contrast the presented elastohydrodynamic framework against two existing approaches, in particular the published RSS methodology of Walker *et al.* (2019) and a resistive force theory (RFT) formulation based on that of Moreau *et al.* (2018). The latter RFT method is as described in the work of Walker *et al.* (2019), although we make use of the resistive coefficients of Hancock (1953) and Gray & Hancock (1955), with the normal resistive coefficient twice that of the tangential coefficient. A detailed comparison of the existing RFT and RSS hydrodynamic methodologies is presented in the work of Walker *et al.* (2019).

https://doi.org/10.1017/jfm.2021.139 Published online by Cambridge University Press

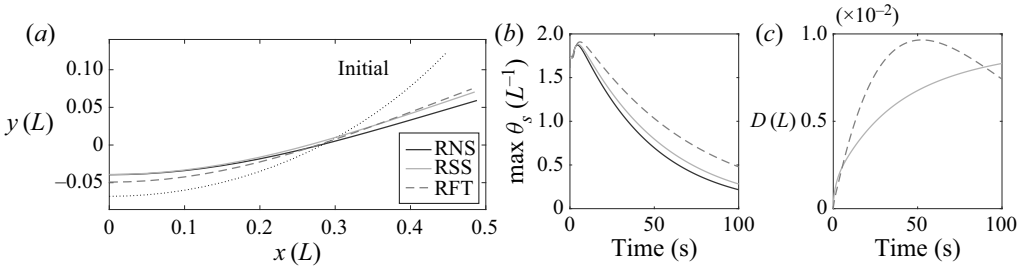


Figure 5. Comparing methodologies via the relaxation of a symmetric filament, simulated with $N = 40$ segments for $E_h = 9600$. Each starting from an initial curved configuration, shown dotted in (*a*), we simulate the relaxation dynamics via RFT, RSS and RNS methodologies. (*a*) Shown at the same instant in time (30 s) are the filament configurations as computed by the three methodologies, with the filament shapes broadly similar although showing some minor differences. Only half of the filament is shown, appealing to the preserved symmetry, and the shared initial condition is shown as a dotted curve. (*b*) The maximum filament curvature as a function of time, highlighting greater distinctions between the methodologies. (*c*) The difference between filament configurations at time t, defined by $D^2 = \int \|\boldsymbol{x}_O - \boldsymbol{x}_{RNS}\|_2^2 \, \mathrm{d}s/L$, quantifies the difference between the RNS method, denoted $\boldsymbol{x}_{RNS}$, and the results of the other frameworks, denoted $\boldsymbol{x}_O$. With a filament aspect ratio of 1 : 100 here, overall differences between computations appear only slight, with the exception of the longer time scale of the RFT solution compared to the non-local methodologies. In the RNS framework, we have considered a filament with dimensionless shape $\eta(s') = \sqrt{1 - s'^2}$, corresponding to a prolate ellipsoid, although note that this information is not captured by the RFT or RSS frameworks.

4.3.1. *A relaxing filament*

We simulate the free relaxation of a bent filament, with the θ_i initially equally spaced and increasing between $-\pi/4$ and $\pi/4$ to correspond to a filament of constant curvature, via each of the three methodologies, picking a common but arbitrary elastohydrodynamic number of $E_h = 9600$ and setting $N = 40$. The filament has aspect ratio 1 : 100, corresponding to $\epsilon = 0.02$ in the RNS framework and $\epsilon = 0.01$ in the RFT and RSS approaches. Simulating until a dimensional time of 100 s, at which point the RNS solution is nearing complete relaxation to a straight configuration, we display snapshots of the computed solutions and some associated metrics in figure 5. Immediately evident is a qualitative similarity between the computations, though there is some pairwise disagreement throughout the motion. Most prominent are differences in the time scale of relaxation, as can be seen in the maximum curvature plot of figure 5(*b*), with the RFT solution relaxing more slowly than the predictions by non-local theories. We more concretely quantify the overall differences between methodologies at a given time t via the measure D, defined for a computed solution $\boldsymbol{x}(s, t)$ by

$$D(t)^2 = \frac{1}{L} \int_0^L \|\boldsymbol{x}(s, t) - \boldsymbol{x}_{RNS}(s, t)\|_2^2 \, \mathrm{d}s, \tag{4.3}$$

relative to the RNS solution $\boldsymbol{x}_{RNS}$. The evolution of this distance measure for the RFT and RSS approaches is shown in figure 5(*c*), and demonstrates that, whilst differences between solutions are indeed small, being on the scale of ϵ in this particular case, these distinctions persist throughout the motion.

With elastohydrodynamic simulations appearing broadly similar at the level of detail considered thus far, we also note a common computational efficiency of the frameworks, with even the more complex regularised non-uniform segments approach computing the relaxation dynamics in a number of seconds. Indeed, this is replicated throughout further

https://doi.org/10.1017/jfm.2021.139 Published online by Cambridge University Press

testing for each of a wide array of initial conditions, and is robust to variations in the radius function $\eta(s')$ and the filament aspect ratio. Thus, despite employing a more sophisticated slender-body ansatz, we see retained in the RNS methodology the desirable efficiency associated with the existing coarse-grained frameworks.

4.3.2. *A simple filament in flow*

From the agreement seen above in the case of a relaxing filament, one might expect that the theoretical refinement offered by the RNS approach over the simpler and cruder RSS methodology is minimal in practice. However, more significant differences are indeed present.

We consider perhaps the most simple possible filament simulation: the dynamics of an initially straight filament in a uniform background flow, with a background flow $\boldsymbol{u}_b$ incorporated into the current framework via the mapping $\boldsymbol{u} \mapsto \boldsymbol{u} - \boldsymbol{u}_b$ as in the work of Walker *et al.* (2019). The simulated filament should exhibit trivial motion and deformation, merely translating with the background flow and retaining its straight configuration. Both the RNS and RSS methodologies successfully replicate this behaviour, and solution time is negligible. However, a noted issue of methods based on regularised Stokeslet segments and similar approaches are endpoint oscillations in the computed force density $\boldsymbol{f}$, present in each of the works of Cortez (2018), Walker *et al.* (2019) and Hall-McNair *et al.* (2019), which persist even with mesh refinement.

Here, we explicitly compute the force density on a straight filament of aspect ratio 1 : 100 in a unit background flow $\boldsymbol{u}_b = \boldsymbol{e}_y$ using both the RNS and RSS approaches, where $\boldsymbol{e}_y$ is perpendicular to the filament tangent. In figure 6(*a–c*) we present the magnitude of the computed force density on the filament from $s = 0$ to $s = L$ for various body radius functions, appealing to symmetry and noting that the force density is identically zero in the direction of the filament tangent. In each case, we observe the oscillations of the RSS force density near the endpoints of the slender body, with the RSS solution being fundamentally independent of the radius function, whilst the piecewise-constant RNS solution essentially eliminates these oscillations. We have taken $N = 200$ in figure 6(*c*) in order to capture the highly oscillatory radius function of figure 3(*c*), consistent with the error analysis of § 3.3, taking $N = 100$ in the other cases.

Perhaps more pertinent, and indeed the motivation behind the use of the ansatz of Walker *et al.* (2020*a*), is the velocity boundary condition on the filament. We explicitly evaluate the flow velocity on the surface of the filament via both the RNS and RSS methods, sampling at 1000 uniformly spaced points on the surface, and show the infinity norm error in the computed velocity in figure 6(*d–f*) as a function of dimensionless shifted arclength s'. Notably, the RSS approach is consistently inaccurate along the length of the slender body, yielding approximately 5 % errors over the entire surface, corresponding to five times the regularisation parameter of the RSS method. The RNS methodology significantly improves upon this, with limitingly small error along the majority of each of the slender bodies in both figures 6(*d*) and 6(*e*), with errors of approximately 2ϵ near the endpoints of the slender body in figure 6(*e*). In particular, these errors are of the same order as those found in the original evaluation of the slender-body theory by Walker *et al.* (2020*a*), with the impact of moving away from quadrature therefore minimal in all but figure 6(*f*), which is improved by reducing Δs to once again accommodate the oscillatory radius function. Thus, we observe that the use of the RNS methodology affords significant gains in the accuracy of the no-slip boundary condition over other approaches. Convergence of this velocity error as a function of N and ϵ is illustrated in Appendix E for the case of figure 3(*b*).

https://doi.org/10.1017/jfm.2021.139 Published online by Cambridge University Press

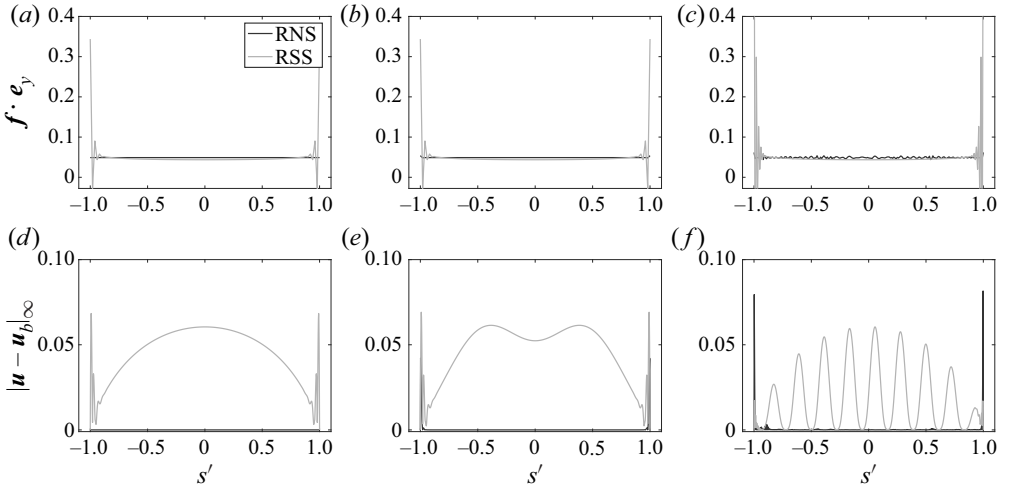


Figure 6. The computed force densities and errors in surface velocity for straight filaments in unit uniform flow, with shapes corresponding to figure 3. Here, we have used an aspect ratio of 1 : 100, corresponding to $\epsilon = 0.02$ for the RNS methodology, and we recall that the slender-body theory upon which it is based is accurate to $O(\epsilon)$. In (*a–c*) we note the presence of significant oscillations near the ends of the filament for the RSS solution, absent from the RNS computation. (*d–f*) We report the error in the surface velocity for a unit magnitude background flow $\boldsymbol{u}_b = \boldsymbol{e}_y$, from which we note the significant improvement in accuracy afforded by the RNS methodology over the RSS approach. In particular, the RNS error is at least an order of magnitude less than the RSS error, except perhaps at the very endpoints of the filament, with the RSS methodology making little systematic attempt to satisfy the boundary condition on the surface. We have taken $N = 100$ in (*a*,*b*,*d*,*e*), whilst in (*c*,*f*) we have taken $N = 200$, with the highly curved radius function of figure 3(*c*) requiring reduced Δs to yield comparable accuracy to the other, simpler cases. (*a*,*d*), (*b*,*e*) and (*c*,*f*) correspond to the shapes shown in (*a*), (*b*) and (*c*) of figure 3.

5. Discussion

Although the study of Moreau *et al.* (2018) vastly increased the computational efficiency of filament simulations, it did so whilst employing resistive force theory, with this leading-order hydrodynamic relation typically conferring errors logarithmic in the filament aspect ratio. Subsequent works have extended this framework to feature improved hydrodynamics (Hall-McNair *et al.* 2019; Walker *et al.* 2019), each making use of a simple but non-local regularised ansatz. However, even these works neglect the boundary condition on the body surface, instead evaluating velocities along the centreline when linking fluid velocity to applied force density. Via the evaluations performed in § 4.3.2 of this work, we have evidenced the relative inaccuracy of such approaches, observing non-negligible errors in the computed surface velocity over the entire length of the slender body, with these hydrodynamic errors being a fundamental weakness of previous methodologies. Incorporating a refined hydrodynamic ansatz, the presented regularised non-uniform segment methodology significantly improves upon such errors, with discrepancies in the velocity boundary condition present only at the filament endpoints, given adequate discretisation to account for the level of variation in the cross-sectional radius function. In particular, the slender-body theory employed here inherently takes into account the complex shape of the filament, enabling the study of realistic slender-body geometries and replacing previous imprecise justifications with analytically derived quantifications of accuracy. Further, we have expanded upon the

https://doi.org/10.1017/jfm.2021.139 Published online by Cambridge University Press

range of geometries permissible in the slender theory of Walker *et al.* (2020*a*), replacing differentiability with weaker continuity assumptions on the regularisation parameter χ.

However, a naive incorporation of the slender-body theory of Walker *et al.* (2020*a*) into a coarse-grained framework of filament elasticity yielded large computation times, sacrificing the efficiency typically associated with the underlying approach of Moreau *et al.* (2018). Indeed, whilst the use of automated quadrature rules allows computation of the hydrodynamic operator to any desired degree of numerical accuracy, the rapidly varying integral kernel of the ansatz of Walker *et al.* (2020*a*) prohibited rapid computation on par with the existing frameworks of Moreau *et al.* (2018), Hall-McNair *et al.* (2019) and Walker *et al.* (2019). Thus, exploiting a low-degree approximation of the unknown force density $\boldsymbol{f}$, we instead computed the necessary integrals analytically, mimicking the approach of Cortez (2018) after Taylor expanding the generally non-quadratic regularisation parameter χ. Quantifying the errors associated with this approximation, we have evidenced a remarkable accuracy and efficiency of this approach, yielding a scheme for elastohydrodynamic simulation that is comparable in computational cost to existing methodologies, whilst simultaneously improving on their accuracy. Thus, the presented framework will enable rapid solution of the forward elastohydrodynamic problem, pertinent to modern Bayesian parameter inference techniques, for example, along with explorations of fluid–structure interactions in slender-body systems. Further, the method of RNS will more generally enable rapid application of the slender-body theory of Walker *et al.* (2020*a*), facilitating future investigative and explorative studies into filament dynamics.

Whilst efficiency gains were made by adopting the general principle of the method of regularised Stokeslet segments, the regularised non-uniform segment approach avoids a pertinent issue associated with the principles of the former theory. Present in the works and published codes of Cortez (2018), Walker *et al.* (2019) and Hall-McNair *et al.* (2019) are severe variations in the computed force density $\boldsymbol{f}$ near the endpoints of the considered filaments, persisting or indeed worsening with increased refinement of approximation. With force density a fundamental component of such elastohydrodynamic frameworks, these apparent errors may contribute non-negligibly to the simulated dynamics and applications, particularly given the reported significance of distal activity in recent model spermatozoa (Neal *et al.* 2020). Thus, the absence of comparable oscillations in the RNS solutions represents a significant advantage over these existing methodologies. Curiously, the insertion of the slender body theory of Walker *et al.* (2020*a*) alone into the framework of Walker *et al.* (2019) was not sufficient to achieve this, as discovered during the author's initial attempt at formulating the RNS methodology, which differs to the presented approach only by using a piecewise linear discretisation of force density $\boldsymbol{f}$. However, the combination of this improved ansatz and a lower-order discretisation of $\boldsymbol{f}$ successfully removed the unphysical oscillations from the computed solutions, yielding the smooth profiles seen in figure 6, although detailed investigation of the Fredholm integral equation of (1.1) is required in order to ascertain the source of such pervasive errors. Future work may also include trivial extensions to the study of active filaments and general background flows, affording justified accuracy to the wide range of elastohydrodynamic problems made tractable by the work of Moreau *et al.* (2018).

In summary, we have integrated the fundamental advance of Moreau *et al.* (2018) and the regularised slender-body theory of Walker *et al.* (2020*a*), overcoming their respective shortfalls to yield a framework for the efficient and accurate simulation of slender-body elastohydrodynamics. The so-called regularised non-uniform segment approach retains the flexibility of its parent models, and hence may be applied to a wide variety of biological

https://doi.org/10.1017/jfm.2021.139 Published online by Cambridge University Press

and biophysical problems to afford increased accuracy over earlier approaches. Further, complex axisymmetric geometries may now be reliably modelled using this framework, previously only realisable with reduced fidelity or drastically increased computational effort. Applicable even more generally, this study has markedly improved the efficiency of the slender-body theory of Walker *et al.* (2020*a*), with this work overall facilitating both the accurate quantification and large-scale no-slip simulation of slender elasticity and hydrodynamics.

Funding. B.J.W. is supported by the UK Engineering and Physical Sciences Research Council (EPSRC), grant EP/N509711/1. The research materials supporting this publication can be accessed at https://doi.org/10.5287/bodleian:jxrYkJazd.

Declaration of interests. The authors report no conflict of interest.

Author ORCIDs.
B.J. Walker https://orcid.org/0000-0003-0853-267X.

Appendix A. Moment balance as a linear system

For $i = 1, \ldots, N$, the rows $\boldsymbol{B}_{i+2}$ of $\boldsymbol{B}$ encode the integrated moment balance in terms of the $\boldsymbol{f}_j$, resultant of integrating over segments i through N. For each i, the summation of (3.4) may be written simply as

$$\sum_{j=i}^{N} \boldsymbol{I}_j \tag{A1}$$

for integrals $\boldsymbol{I}_j$. For $j = 2, \ldots, N-1$, these are given by

$$\boldsymbol{I}_j = \frac{\Delta s}{2}\left[\boldsymbol{x}_j - \boldsymbol{x}_i - \frac{1}{4}\boldsymbol{v}_j\right] \times \boldsymbol{f}_j + \frac{\Delta s}{2}\left[\boldsymbol{x}_j - \boldsymbol{x}_i - \frac{3}{4}\boldsymbol{v}_j\right] \times \boldsymbol{f}_{j+1}, \tag{A2}$$

where $\boldsymbol{v}_j = \boldsymbol{x}_j - \boldsymbol{x}_{j+1}$. For $j = 1$, again writing $d = L(1-e)/(2\Delta s)$, we have the modified expression

$$\begin{aligned}\boldsymbol{I}_1 = {} & \frac{\Delta s}{2}\left[(1+d)(\boldsymbol{x}_j - \boldsymbol{x}_i) - \frac{1}{4}(1+d)^2\boldsymbol{v}_1\right] \times \boldsymbol{f}_1 \\ & + \frac{\Delta s}{2}\left[(1-d)(\boldsymbol{x}_j - \boldsymbol{x}_i) + \left(\frac{1}{4}(1+d)^2 - 1\right)\boldsymbol{v}_1\right] \times \boldsymbol{f}_2,\end{aligned} \tag{A3}$$

whilst for $j = N$ we have

$$\begin{aligned}\boldsymbol{I}_N = {} & \frac{\Delta s}{2}\left[(1-d)(\boldsymbol{x}_j - \boldsymbol{x}_i) - \frac{1}{4}(1-d)^2\boldsymbol{v}_N\right] \times \boldsymbol{f}_N \\ & + \frac{\Delta s}{2}\left[(1+d)(\boldsymbol{x}_j - \boldsymbol{x}_i) + \left(\frac{1}{4}(1-d)^2 - 1\right)\boldsymbol{v}_N\right] \times \boldsymbol{f}_{N+1}.\end{aligned} \tag{A4}$$

These expressions are self-consistent, as taking $d = 0$ in the latter two yields the expression for $\boldsymbol{I}_j$.

https://doi.org/10.1017/jfm.2021.139 Published online by Cambridge University Press

Appendix B. Choices of mollifier

In order to generate the regularised Stokeslet and potential dipole of (3.17) and (3.18), we employ the mollifiers ϕ^S_χ and ϕ^D_χ, respectively. For a displacement $\boldsymbol{x}$, these are defined as

$$\phi^S_\chi(\boldsymbol{x}) = \frac{15\chi^2}{8\pi(|\boldsymbol{x}|^2+\chi)^{7/2}}, \quad \phi^D_\chi(\boldsymbol{x}) = \frac{3\chi}{4\pi(|\boldsymbol{x}|^2+\chi)^{5/2}}, \tag{B1a,b}$$

following Cortez (2001) and Ainley *et al.* (2008), to which we direct the interested reader for full details and the derivation of the resulting expressions.

Appendix C. Integrals as a linear combination

We decompose the integral of (3.24) over a straight segment with endpoints $\boldsymbol{x}_j$ and $\boldsymbol{x}_{j+1}$, adopting a piecewise-constant discretisation of the force density $\boldsymbol{f}$, such that it takes the value $\boldsymbol{f}_j$ on the half of the segment nearest to $\boldsymbol{x}_j$, and $\boldsymbol{f}_{j+1}$ otherwise. The limits of integration are determined by seeking either the coefficient of $\boldsymbol{f}_j$ or that of $\boldsymbol{f}_{j+1}$, and for brevity we omit such limits here and will refer instead to the placeholder $T_{m,q}$ in lieu of $T^L_{m,q}$ and $T^R_{m,q}$ in what follows, which should be appropriately substituted. Parameterising the straight segment by $\alpha \in [0,1]$, with $\boldsymbol{x}(\alpha) = \boldsymbol{x}_j - \alpha\boldsymbol{v}$, where $\boldsymbol{v} = \boldsymbol{x}_j - \boldsymbol{x}_{j+1}$, and taking $\boldsymbol{K}^\chi$ to be the kernel of (3.24), we may write the integral over the part of the segment as

$$\int \boldsymbol{K}^\chi(\boldsymbol{x}, s')\boldsymbol{f}(s')\,\mathrm{d}s' = \boldsymbol{K}^\chi_I \boldsymbol{f}^\star, \tag{C1}$$

where $\boldsymbol{f}^\star$ is the constant force density over the domain of integration, which is either $\alpha \in [0, 1/2]$ or $\alpha \in [1/2, 1]$. The operator $\boldsymbol{K}^\chi_I$ is given explicitly by

$$\boldsymbol{K}^\chi_I = |\boldsymbol{v}|\left(\boldsymbol{K}_{\boldsymbol{S}} - \frac{1-e^2}{2e^2}\left[(e^2 - s_j'^2)\boldsymbol{K}_{\boldsymbol{D}_0} - 2s_j'|\boldsymbol{v}|\,\boldsymbol{K}_{\boldsymbol{D}_1} - |\boldsymbol{v}|^2\,\boldsymbol{K}_{\boldsymbol{D}_2}\right]\right), \tag{C2}$$

where the outermost $|\boldsymbol{v}|$ term arises due to the change of integration variable from s' to α. In turn, the terms $\boldsymbol{K}_{\boldsymbol{S}}, \boldsymbol{K}_{\boldsymbol{D}_0}, \boldsymbol{K}_{\boldsymbol{D}_1}, \boldsymbol{K}_{\boldsymbol{D}_2}$ are given by

$$\boldsymbol{K}_{\boldsymbol{S}} = +\boldsymbol{C}_{0,1}T_{0,-1} + 1(\boldsymbol{C}_{0,3}T_{0,-3} + \boldsymbol{C}_{1,3}T_{1,-3} + \boldsymbol{C}_{2,3}T_{2,-3}), \tag{C3}$$

$$\boldsymbol{K}_{\boldsymbol{D}_0} = -\boldsymbol{C}_{0,1}T_{0,-3} + 3(\boldsymbol{C}_{0,3}T_{0,-5} + \boldsymbol{C}_{1,3}T_{1,-5} + \boldsymbol{C}_{2,3}T_{2,-5}), \tag{C4}$$

$$\boldsymbol{K}_{\boldsymbol{D}_1} = -\boldsymbol{C}_{0,1}T_{1,-3} + 3(\boldsymbol{C}_{0,3}T_{1,-5} + \boldsymbol{C}_{1,3}T_{2,-5} + \boldsymbol{C}_{2,3}T_{3,-5}), \tag{C5}$$

$$\boldsymbol{K}_{\boldsymbol{D}_2} = -\boldsymbol{C}_{0,1}T_{2,-3} + 3(\boldsymbol{C}_{0,3}T_{2,-5} + \boldsymbol{C}_{1,3}T_{3,-5} + \boldsymbol{C}_{2,3}T_{4,-5}). \tag{C6}$$

Finally, the coefficients $C_{0,1}, C_{0,3}, C_{1,3}, C_{2,3}$ are determined by the choice of Taylor expansion point, being either the left or right endpoint of the segment. When expanding about the left endpoint, where the shifted rescaled arclength parameter is s'_j, we have

$$\boldsymbol{C}_{0,1} = \boldsymbol{I}, \tag{C7}$$

$$\boldsymbol{C}_{0,3} = \chi(s'_j)\boldsymbol{I} + \boldsymbol{w}\boldsymbol{w}^T, \tag{C8}$$

$$\boldsymbol{C}_{1,3} = |\boldsymbol{v}|\frac{\mathrm{d}\chi}{\mathrm{d}s'}(s'_j)\boldsymbol{I} + \boldsymbol{w}\boldsymbol{v}^T + \boldsymbol{v}\boldsymbol{w}^T, \tag{C9}$$

$$\boldsymbol{C}_{2,3} = \frac{1}{2}|\boldsymbol{v}|^2\frac{\mathrm{d}^2\chi}{\mathrm{d}s'^2}(s'_j)\boldsymbol{I} + \boldsymbol{v}\boldsymbol{v}^T, \tag{C10}$$

with $\boldsymbol{v}$ as defined previously. Here, $\boldsymbol{w}$ joins the evaluation point to the left endpoint of the segment, which, in the case of (3.24), is given as $\boldsymbol{w} = \boldsymbol{x}^S(s'_i, \phi) - \boldsymbol{x}_j$ but may be

https://doi.org/10.1017/jfm.2021.139 Published online by Cambridge University Press

readily generalised to evaluation points off the surface of the filament. The corresponding expressions for expansion about the right endpoint are

$$\boldsymbol{C}_{0,1} = \boldsymbol{I}, \tag{C11}$$

$$\boldsymbol{C}_{0,3} = \left(\chi(s'_{j+1}) - |\boldsymbol{v}| \frac{\mathrm{d}\chi}{\mathrm{d}s'}(s'_{j+1}) + \frac{1}{2}|\boldsymbol{v}|^2 \frac{\mathrm{d}^2\chi}{\mathrm{d}s'^2}(s'_{j+1}) \right) \boldsymbol{I} + \boldsymbol{w}\boldsymbol{w}^T, \tag{C12}$$

$$\boldsymbol{C}_{1,3} = \left(|\boldsymbol{v}| \frac{\mathrm{d}\chi}{\mathrm{d}s'}(s'_{j+1}) - |\boldsymbol{v}|^2 \frac{\mathrm{d}^2\chi}{\mathrm{d}s'^2}(s'_{j+1}) \right) \boldsymbol{I} + \boldsymbol{w}\boldsymbol{v}^T + \boldsymbol{v}\boldsymbol{w}^T, \tag{C13}$$

$$\boldsymbol{C}_{2,3} = \frac{1}{2}|\boldsymbol{v}|^2 \frac{\mathrm{d}^2\chi}{\mathrm{d}s'^2}(s'_{j+1})\boldsymbol{I} + \boldsymbol{v}\boldsymbol{v}^T. \tag{C14}$$

Appendix D. Explicit antiderivatives

Writing $\beta = \beta(\alpha) = B + 2C\alpha$ for brevity, the antiderivatives of $\alpha^m R^q$ for $m = 0, q \in \{-1, -3, -5\}$ may be readily computed as

$$\int R^{-1}\,\mathrm{d}\alpha = C^{-1/2}\log\left(\beta + 2C^{1/2}R(\alpha)\right), \tag{D1}$$

$$\int R^{-3}\,\mathrm{d}\alpha = -\frac{2}{B^2 - 4AC}\frac{\beta}{R(\alpha)}, \tag{D2}$$

$$\int R^{-5}\,\mathrm{d}\alpha = -\frac{2}{3(B^2 - 4AC)^2}\frac{(B^2 - 8BC\alpha - 4C(3A + 2C\alpha^2))\beta}{R(\alpha)^3}, \tag{D3}$$

unless we are in the degenerate case, where $B^2 - 4AC = 0$, which yields

$$\int R^{-1}\,\mathrm{d}\alpha = C^{-1/2}\mathrm{sgn}(\beta)\log(\beta), \tag{D4}$$

$$\int R^{-3}\,\mathrm{d}\alpha = -2C^{1/2}\frac{\mathrm{sgn}(\beta)}{\beta^2}, \tag{D5}$$

$$\int R^{-5}\,\mathrm{d}\alpha = -4C^{3/2}\frac{\mathrm{sgn}(\beta)}{\beta^4}. \tag{D6}$$

Here, we have assumed that $C > 0$, consistent with our assumptions on the derivatives of χ and the definition of C in (3.30*a–c*). The analysis of Walker *et al.* (2020*a*) and the assumptions of (3.29) are sufficient to guarantee that the $R(\alpha)$ is non-zero on $\alpha \in [0, 1]$; thus, these integrals are indeed well defined.

Appendix E. Convergence of surface velocity

For the radius function in figure 3(*b*), we compute the error in the surface velocity of a straight filament in unit background flow using the RNS methodology, as in § 4.3.2 although here sampling at 2000 points on the surface. The maximum error over the filament surface is reported in figure 7, showing substantial refinement as N increases for common values of slenderness parameter ϵ. Similar to the method of regularised Stokeslet segments (Cortez 2018; Walker *et al.* 2019), for regimes with both large ϵ and N we see that the error increases dramatically, such that the method is highly inaccurate, occurring when the parameters are

https://doi.org/10.1017/jfm.2021.139 Published online by Cambridge University Press

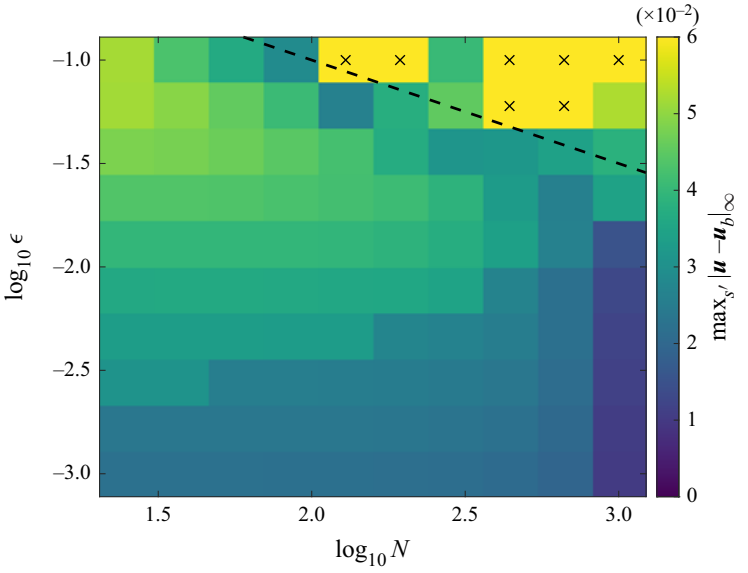


Figure 7. Surface velocity error as a function of slenderness parameter and discretisation. We compute the maximum infinity norm error in the surface velocity over 2000 points for a straight filament with radius function as in figure 3(*b*) and a unit background flow $\boldsymbol{u}_b = \boldsymbol{e}_y$ using the method of regularised non-uniform segments. We show in colour the error as a function of ϵ and N, with convergence apparent as N increases for most common values of ϵ. For both ϵ and N large, we see a drastic increase in error, approximately in the region bounded below by the black dashed line, which is empirically given as $\epsilon\sqrt{N} = 1$. Sections marked with a cross exhibit errors significantly larger than the range of the colour axis, although these also lie outside parameter regimes of typical relevance.

approximately past the threshold $\epsilon\sqrt{N} = 1$, which is illustrated as a black dashed line in figure 7, although this relation is purely empirical. Notably, this typical breakdown occurs outside regimes of common relevance. Regions marked with crosses correspond to errors larger than the range of the colour axis.

References

Ainley, J., Durkin, S., Embid, R., Boindala, P. & Cortez, R. 2008 The method of images for regularized Stokeslets. *J. Comput. Phys.* **227** (9), 4600–4616.

Chwang, A.T. & Wu, T.Y.-T. 1975 Hydromechanics of low-Reynolds-number flow. Part 2. Singularity method for Stokes flows. *J. Fluid Mech.* **67** (4), 787–815.

Cortez, R. 2001 The method of regularized Stokeslets. *SIAM J. Sci. Comput.* **23** (4), 1204–1225.

Cortez, R. 2018 Regularized Stokeslet segments. *J. Comput. Phys.* **375**, 783–796.

Cortez, R. & Nicholas, M. 2012 Slender body theory for Stokes flows with regularized forces. *Commun. Appl. Maths Comput. Sci.* **7** (1), 33–62.

Cox, R.G. 1970 The motion of long slender bodies in a viscous fluid Part 1. General theory. *J. Fluid Mech.* **44** (04), 791–810.

Curtis, M.P., Kirkman-Brown, J.C., Connolly, T.J. & Gaffney, E.A. 2012 Modelling a tethered mammalian sperm cell undergoing hyperactivation. *J. Theor. Biol.* **309**, 1–10.

Gillies, E.A., Cannon, R.M., Green, R.B. & Pacey, A.A. 2009 Hydrodynamic propulsion of human sperm. *J. Fluid Mech.* **625**, 445–474.

Gray, J. 1928 *Ciliary Movement*. Cambridge University Press.

Gray, J. & Hancock, G.J. 1955 The propulsion of sea-urchin spermatozoa. *J. Exp. Biol.* **32** (4), 802–814.

Guglielmini, L., Kushwaha, A., Shaqfeh, E.S.G. & Stone, H.A. 2012 Buckling transitions of an elastic filament in a viscous stagnation point flow. *Phys. Fluids* **24** (12), 123601.

https://doi.org/10.1017/jfm.2021.139 Published online by Cambridge University Press

HALL-MCNAIR, A.L., MONTENEGRO-JOHNSON, T.D., GADÊLHA, H., SMITH, D.J. & GALLAGHER, M.T. 2019 Efficient implementation of elastohydrodynamics via integral operators. *Phys. Rev. Fluids* **4** (11), 1–24.

HANCOCK, G.J. 1953 The self-propulsion of microscopic organisms through liquids. *Proc. R. Soc. Lond.* A **217** (1128), 96–121.

ISHIMOTO, K. & GAFFNEY, E.A. 2018 An elastohydrodynamical simulation study of filament and spermatozoan swimming driven by internal couples. *IMA J. Appl. Maths* **83** (4), 655–679.

JOHNSON, R.E. 1980 An improved slender-body theory for Stokes flow. *J. Fluid Mech.* **99** (2), 411–431.

KELLER, J.B. & RUBINOW, S.I. 1976 Slender-body theory for slow viscous flow. *J. Fluid Mech.* **75** (4), 705–714.

LIGHTHILL, J. 1976 Flagellar hydrodynamics. *SIAM Rev.* **18** (2), 161–230.

MOREAU, C., GIRALDI, L. & GADÊLHA, H. 2018 The asymptotic coarse-graining formulation of slender-rods, bio-filaments and flagella. *J. R. Soc. Interface* **15** (144), 20180235.

NEAL, C.V., HALL-MCNAIR, A.L., KIRKMAN-BROWN, J., SMITH, D.J. & GALLAGHER, M.T. 2020 Doing more with less: the flagellar end piece enhances the propulsive effectiveness of human spermatozoa. *Phys. Rev. Fluids* **5** (7), 073101.

OLSON, S.D., LIM, S. & CORTEZ, R. 2013 Modeling the dynamics of an elastic rod with intrinsic curvature and twist using a regularized Stokes formulation. *J. Comput. Phys.* **238**, 169–187.

POZRIKIDIS, C. 1992 *Boundary Integral and Singularity Methods for Linearized Viscous Flow*. Cambridge University Press.

POZRIKIDIS, C. 2010 Shear flow over cylindrical rods attached to a substrate. *J. Fluids Struct.* **26** (3), 393–405.

ROPER, M., DREYFUS, R., BAUDRY, J., FERMIGIER, M., BIBETTE, J. & STONE, H.A. 2006 On the dynamics of magnetically driven elastic filaments. *J. Fluid Mech.* **554**, 167–190.

DU ROURE, O., LINDNER, A., NAZOCKDAST, E.N. & SHELLEY, M.J. 2019 Dynamics of flexible fibers in viscous flows and fluids. *Annu. Rev. Fluid Mech.* **51** (1), 539–572.

SCHOELLER, S.F. & KEAVENY, E.E. 2018 From flagellar undulations to collective motion: predicting the dynamics of sperm suspensions. *J. R. Soc. Interface* **15** (140), 20170834.

SHAMPINE, L.F. & REICHELT, M.W. 1997 The MATLAB ODE suite. *SIAM J. Sci. Comput.* **18** (1), 1–22.

SIMONS, J., FAUCI, L. & CORTEZ, R. 2015 A fully three-dimensional model of the interaction of driven elastic filaments in a Stokes flow with applications to sperm motility. *J. Biomech.* **48** (9), 1639–1651.

SMITH, D.J. 2009 A boundary element regularized Stokeslet method applied to cilia- and flagella-driven flow. *Proc. R. Soc. Lond.* A **465** (2112), 3605–3626.

SMITH, D.J., MONTENEGRO-JOHNSON, T.D. & LOPES, S.S. 2019 Symmetry-breaking cilia-driven flow in embryogenesis. *Annu. Rev. Fluid Mech.* **51** (1), 105–128.

TORNBERG, A.K. & SHELLEY, M.J. 2004 Simulating the dynamics and interactions of flexible fibers in Stokes flows. *J. Comput. Phys.* **196** (1), 8–40.

WALKER, B.J., CURTIS, M.P., ISHIMOTO, K. & GAFFNEY, E.A. 2020*a* A regularised slender-body theory of non-uniform filaments. *J. Fluid Mech.* **899**, A3.

WALKER, B.J., ISHIMOTO, K. & GAFFNEY, E.A. 2020*b* Efficient simulation of filament elastohydrodynamics in three dimensions. *Phys. Rev. Fluids* **5** (12), 123103.

WALKER, B.J., ISHIMOTO, K., GADÊLHA, H. & GAFFNEY, E.A. 2019 Filament mechanics in a half-space via regularised Stokeslet segments. *J. Fluid Mech.* **879**, 808–833.

https://doi.org/10.1017/jfm.2021.139 Published online by Cambridge University Press